PERGAMON

International Journal of Heat and Mass Transfer 44 (2001) 1185–1199

International Journal of HEAT and MASS TRANSFER

www.elsevier.com/locate/ijhmt

Isothermal and heated turbulent upflow in a vertical annular channel – Part II. Numerical simulations

J.A. Zarate [a], R.P. Roy [a,*], A. Laporta [b]

[a] Department of Mechanical and Aerospace Engineering, Arizona State University, Mail Station 6106, Tempe, AZ 85287-6106, USA
[b] Electricité de France, Departement Transferts Thermiques et Aerodynamiques, Chatou, France

Received 28 September 1999; received in revised form 28 April 2000

Abstract

Numerical simulations of isothermal and heated turbulent upflow of a liquid in a vertical concentric annular channel with its inner wall heated were carried out. Near-wall two-equation turbulence models were used to close the Reynolds-averaged momentum and thermal energy equations. In addition, a near-wall explicit turbulent heat flux model was incorporated. The results reported include mean and turbulence quantities. Comparison with our measurements reported in Part I of this two-part paper is presented. The Reynolds number at the channel inlet ranged from 22 800 to 46 400, and the range of Gr/Re^2 at the measurement plane was 0.009–0.078. Buoyancy effects which influenced the velocity and thermal fields were observed in the simulation results as they were in the measurements.

1. Introduction

A number of numerical studies of turbulent flow in concentric annular channels at isothermal and heated conditions have been reported. In the following, some of them are reviewed.

Quarmby [1] carried out an analysis of isothermal flow in a concentric annular channel using the Reynolds number and radius ratio of the channel as parameters. Results reported included the friction factor, the velocity wall laws for the inner and outer walls, and the maximum mean axial velocity location. Hanjalic [2] simulated isothermal turbulent flow in a concentric annulus using high Reynolds number versions of the transport equations for axial turbulent shear stress, turbulent kinetic energy, and its dissipation rate. The wall boundary conditions for the mean and turbulence quantities were imposed by means of a modified velocity wall law in which the additive constant is a function of the radius ratio r_i/r_o. Azous et al. [3] simulated isothermal flow in concentric and eccentric annuli using a low-Reynolds number two-equation k–τ model of turbulence and a mixing length model as closures.

Numerical simulation of the velocity and thermal fields in turbulent flow through a concentric annular channel with its inner wall heated was performed by Wilson and Medwell [4], and Malik and Pletcher [5]. Wilson and Medwell [4] used the van Driest model of turbulent viscosity which takes into account the viscous damping in the near-wall region. A constant turbulent Prandtl number, $Pr_t = 1$, was used for $Pr \geqslant 0.1$ and an empirical relation for Pr_t due to Deissler was adopted for $Pr < 0.1$. Three different turbulence models to evaluate the eddy viscosity and a constant turbulent Prandtl number of 0.9 were used by Malik and Pletcher [5].

Mixed convection flow in channels has been studied numerically and experimentally by several researchers. Petukhov and Polyakov [6] presented a comprehensive discussion of turbulent mixed convection in wall-bounded flows. They suggested that buoyancy forces affect the velocity field in two ways – the *external effect* which acts on the whole flow field because of the non-homogeneous fluid density distribution and the *structural effect* which arises from fluctuating fluid density in the gravity field and modifies the turbulence directly.

* Corresponding author. Tel.: +1-480-965-1482; fax: +1-480-963-1384.
E-mail address: roy@asu.edu (R.P. Roy).

0017-9310/01/$ - see front matter
PII: S0017-9310(00)00151-4

Nomenclature

A, A^+	constant, model parameter that is a function of Pr
$C_{d1}, C_{d2}, C_{d3}, C_{d4}, C_{d5}$	model constants in the ϵ_t equation
$C_{\epsilon 1}, C_{\epsilon 2}, C_{\epsilon 3}$	model constants in the ϵ equation
$C_\lambda, C_{\lambda 1}$	model constant, model parameter that is a function of Pr
C_μ	model constant
C_P	specific heat at constant pressure
C_{1t}, C_{2t}	model constants in the equations for $\overline{u_i t}$
D_h	channel hydraulic diameter, $2(r_o - r_i)$
f_{w1}	near-wall damping function in the equation for ϵ, $\exp[-(Re_t/40)^2]$
f_{wet}	near-wall damping function in the equation for ϵ_t, $\exp[-(Re_t/80)^2]$
$f_\lambda, f_{\lambda 1}$	near-wall damping functions in the expression for α_t
f_μ	near-wall damping function for eddy viscosity
g_i	i-component of the acceleration due to gravity
G_k	production/destruction of k due to buoyancy
Gr	Grashof number, $\beta g(\overline{T}_{wi} - \overline{T}_b) D_h^3/\nu^2$
k	turbulent kinetic energy per unit mass of fluid
n_j	j-component of the unit normal vector, positive outward from the wall
P	mean pressure
P_k	production of k due to mean shear
P_t	production of $\overline{t^2}$ due to mean temperature gradients
P_t^*	production of $\overline{t^2}$ due to mean temperature gradient in the streamwise direction
Pr, Pr_t	molecular Prandtl number, turbulent Prandtl number
q''_w	wall heat flux
r	radial coordinate
R^*	dimensionless radius, $(r - r_i)/(r_o - r_i)$
R_m	radial location of maximum mean axial velocity
R_0	radial location of zero axial turbulent shear stress
Re	Reynolds number, $\overline{U}_b D_h/\nu$, based on fluid properties at $\overline{T}_{in}$
Re_t, Re_ϵ	turbulent Reynolds numbers: $k^2/\nu\epsilon, (\nu\epsilon)^{1/4} y/\nu$
S_{ij}	mean strain rate tensor, $1/2(\partial\overline{U}_i/\partial x_j + \partial\overline{U}_j/\partial x_i)$
$\overline{T}, \overline{T}_b, T_\tau$	mean temperature, mean bulk temperature, friction temperature
$\overline{T}_{wi}, \overline{T}_{wo}$	mean temperature at inner wall, outer wall
t	time; also, temperature fluctuation
$t', \overline{t^2}$	temperature fluctuation intensity, variance of temperature fluctuation
$\overline{U}, \overline{U}_b$	mean axial velocity, mean axial bulk velocity at channel inlet
$\overline{U}_i, U_\tau$	i-component of mean velocity; friction velocity, $(\tau_w/\rho)^{1/2}$
$\overline{u^2}, \overline{v^2}, \overline{w^2}$	axial, radial, azimuthal turbulent stresses
u_i	i-component of velocity fluctuation
u'_c	characteristic velocity fluctuation intensity, $(2k/3)^{1/2}$
$\overline{ut}$	axial turbulent heat flux (divided by ρC_P)
$\overline{u_i t}$	i-component of turbulent heat flux vector (divided by ρC_P)
$\overline{u_i u_j}$	turbulent shear stress tensor (divided by ρ)
$\overline{uv}$	axial turbulent shear stress (divided by ρ)
$\overline{vt}$	radial turbulent heat flux (divided by ρC_P)
W_{ij}	mean rotation rate tensor, $1/2(\partial\overline{U}_i/\partial x_j - \partial\overline{U}_j/\partial x_i)$
x_i	coordinates
y, y^+	coordinate normal to the wall, nondimensional wall normal coordinate, yU_τ/ν
z	axial coordinate

Greek symbols

α, α_t	molecular thermal diffusivity, turbulent thermal diffusivity
β	volumetric coefficient of thermal expansion for fluid, $-(1/\rho)(\partial\rho/\partial T)_P$
δ_{ij}	Kronecker delta
ϵ	dissipation rate of k per unit mass of fluid
ϵ_{it}	dissipation rate of the turbulent heat flux vector

$\tilde{\epsilon}$, $\overline{\epsilon}$	modified dissipation rate of k: $\epsilon - 2\nu\left(\partial k^{1/2}/\partial y\right)^2$, $\epsilon - 2\nu k/y^2$	τ	turbulent time scale, k/ϵ
ϵ_t	dissipation rate of $\overline{t^2}$ per unit mass of fluid	τ_{wi}, τ_{wo}	axial shear stress at inner wall, outer wall
$\tilde{\epsilon}_t$, ϵ_t^*	modified dissipation rate of $\overline{t^2}$: $\epsilon_t - \alpha\left[\partial\left(\overline{t^2}\right)^{1/2}\Big/\partial y\right]^2$, $\epsilon_t - \alpha\overline{t^2}/y^2$	ξ	near-wall correction to ϵ equation
		$\xi_{\epsilon t}$	near-wall correction to ϵ_t equation
		Subscripts	
μ, μ_t	dynamic viscosity of fluid, turbulent viscosity	0	reference state; also, zero axial shear stress location
ν, ν_t	kinematic viscosity of fluid, turbulent momentum diffusivity	c	radial location where the heated and isothermal mean axial velocity profiles intersect
Θ	nondimensional temperature, $(\overline{T} - \overline{T}_{wo})/(\overline{T}_{wi} - \overline{T}_{wo})$	i, o	annular channel inner wall, outer wall
ρ	density of fluid	m.p.	measurement plane
σ_k, σ_ϵ, σ_t, $\sigma_{\epsilon t}$	model constants in the equations for: k, ϵ, $\overline{t^2}$, ϵ_t		

Among the authors who have reported numerical simulation of turbulent flow and heat transfer in channels at mixed convection condition using the k–ϵ model of turbulence but did not include buoyancy effects in the turbulence model are Abdelmeguid and Spalding [7], Pyetrzyk and Crawford [8], and Cotton and Jackson [9]. Reynolds analogy (i.e., a turbulent Prandtl number) was invoked to model the turbulent heat flux. Use of a turbulent Prandtl number, typically assigned a constant value, forces a similarity between the turbulent shear stresses and the corresponding turbulent heat fluxes and can lead to large errors even in the prediction of the mean temperature field and integral quantities such as the wall heat transfer coefficient. This is especially the case if the molecular Prandtl number of the fluid is significantly different from unity. Some studies show that Pr_t is a function of the molecular Prandtl number and the distance from the wall, Kays [10]. However, there is no generally accepted relation for this dependence. Furthermore, direct numerical simulation (DNS) results indicate that Pr_t is not constant over the flow field [11].

To remove the assumption of constant Pr_t, two-equation and second-order models of the turbulent temperature field have been proposed. Two-equation models provide an isotropic turbulent thermal diffusivity which depends on the turbulent kinetic energy, its dissipation rate, the variance of temperature fluctuation, and its dissipation rate. The turbulent heat fluxes are then calculated using the gradient transport approximation. In contrast, second-order models provide an equation for each component of the turbulent heat flux vector. From this, it would seem that the more attractive option is the use of a second-order model. However, it is known that the order of the turbulent heat transfer model should be *at most* of the same order as the turbulence model for the velocity field [12]. Therefore, if a k–ϵ model is used for the velocity field, the highest order closure that can be used for the temperature field is a two-equation model.

On the other hand, if a two-equation model is used for the thermal field, it is probable that the turbulent heat flux components will not be predicted correctly. As an example, our measurements presented in Part I of this two-part paper show that there occurs a change of sign in the axial turbulent heat flux across the gap of an annular channel whose inner wall only is heated, and that the magnitude of this heat flux component is often larger than that of the radial component. As a consequence of the gradient transport approximation however, the two-equation model will predict negative axial turbulent heat flux across the entire annular gap. Furthermore, since the axial temperature gradient is small the predicted magnitude of the axial heat flux may be significantly smaller than its actual value. One way to remedy this is to use an algebraic heat flux model which can provide a good approximation to the observed behavior of the turbulent heat flux components.

Several two-equation models of the turbulent temperature field have been proposed during the past decade. Among those are the models of Youssef et al. [13], and So and Sommer [12]. To close the Reynolds-averaged Navier–Stokes (RANS) equations Youssef et al. [13] used a near-wall k–ϵ model. So and Sommer [12] used both near-wall second-order and k–ϵ models as closures for the RANS equations.

Recently, So and Sommer [14] proposed an explicit algebraic heat-flux (EAHF) model which they used in conjunction with their two-equation temperature field model [12] to calculate the turbulent heat flux components. The EAHF model was derived assuming local equilibrium turbulence of the velocity and the thermal

fields, and incorporated the isotropic turbulent thermal diffusivity given by the $\overline{t^2}$–ϵ_t model. The EAHF model was able to capture the anisotropy of the turbulent heat flux components.

We have carried out experiments and computations in turbulent upflow of liquid refrigerant-113 (R-113) through a vertical annular channel of radius ratio 0.415 at isothermal and heated conditions. At the latter condition the inner wall of the annulus was heated and the outer wall insulated, Fig. 1. In this paper, the computational work is reported and its results are compared with the experimental data presented in the Part I paper.

The RANS and thermal energy equations were the conservation equations solved numerically. To model the Reynolds stresses and turbulent heat fluxes, equations for turbulent kinetic energy k, its dissipation rate ϵ, the variance of temperature fluctuation $\overline{t^2}$, and its dissipation rate ϵ_t were introduced in their near-wall forms. Away from the walls, these equations approach their respective high Reynolds number forms. Introduction of these turbulence model equations eliminated the need for specifying wall functions and turbulent Prandtl number. In addition, the EAHF model of So and Sommer [14] was incorporated.

Simulations are reported here for the three-channel inlet Reynolds numbers at which experiments were performed, viz., 22 800, 31 500 and 46 400. The range of the buoyancy parameter Gr/Re^2 at the measurement plane of the channel is 0.009–0.078. Although these are low values, our measurements displayed features of

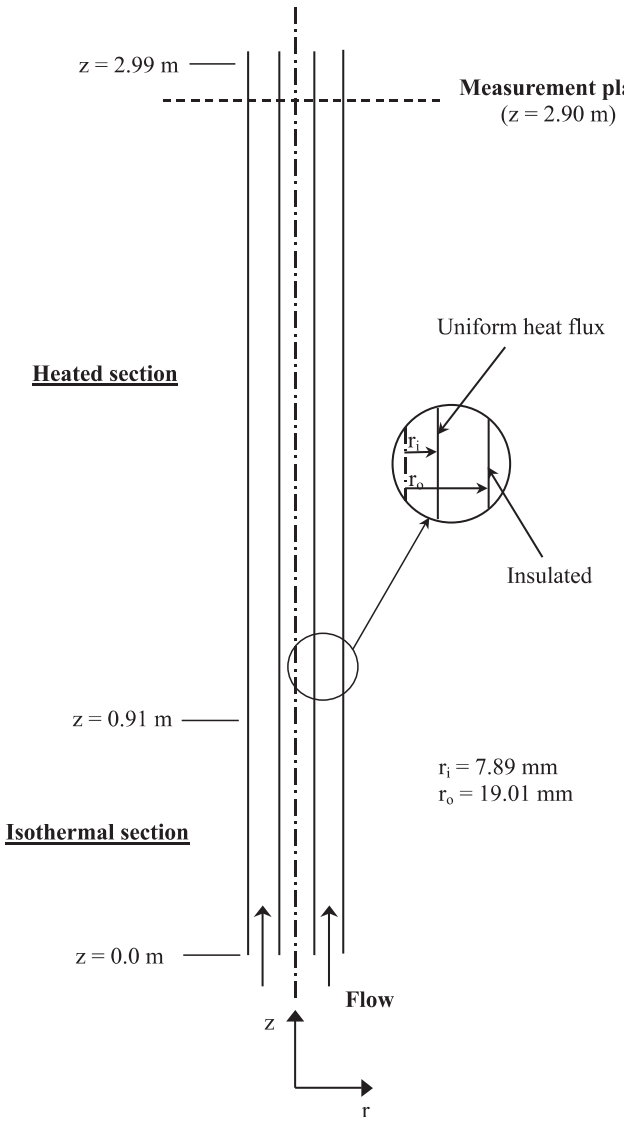

Fig. 1. The annular channel.

turbulent mixed convection. It was, therefore, deemed necessary to include buoyancy effects in the model. To include these effects in the turbulence model, additional terms along with their near-wall corrections were introduced in the transport equations for k and ϵ as well as in the EAHF model [15].

2. Mathematical model

2.1. Conservation equations

The Reynolds-averaged equations for mass, momentum, and thermal energy were the base equations solved. These equations are, in tensorial notation

$$\frac{\partial \rho}{\partial t}+\frac{\partial\left(\rho \overline{U}_j\right)}{\partial x_j}=0, \tag{1}$$

$$\rho\left[\frac{\partial \overline{U}_i}{\partial t}+\overline{U}_j\frac{\partial \overline{U}_i}{\partial x_j}\right]=-\frac{\partial P'}{\partial x_i}+(\rho-\rho_0)g_i+\frac{\partial}{\partial x_j}\left[2\mu S_{ij}-\frac{2}{3}\mu S_{kk}\delta_{ij}-\rho\overline{u_iu_j}\right], \tag{2}$$

$$\rho\left[\frac{\partial \overline{T}}{\partial t}+\overline{U}_j\frac{\partial \overline{T}}{\partial x_j}\right]=\frac{\partial}{\partial x_j}\left[\rho\left(\alpha\frac{\partial \overline{T}}{\partial x_j}-\overline{u_jt}\right)\right]. \tag{3}$$

In the momentum equation, P' is a modified pressure defined as $P'=P-\rho_0 g_i x_i$. ρ_0 is the density of the fluid at a reference state which was chosen to be the channel inlet temperature and pressure. In Eqs. (1)–(3) as well as in the equations presented later, repeated indices mean summation.

2.2. Closure models

2.2.1. Velocity field

For closing the momentum equations, the Reynolds stress tensor $\overline{u_iu_j}$ has to be provided. $\overline{u_iu_j}$ was calculated on the basis of the eddy viscosity hypothesis

$$\overline{u_iu_j}=-2\nu_t S_{ij}+\frac{2}{3}\delta_{ij}\nu_t S_{mm}+\frac{2}{3}\delta_{ij}k. \tag{4}$$

The turbulent momentum diffusivity was calculated from the turbulent kinetic energy k and its dissipation rate ϵ. The near-wall k–ϵ model proposed by Sarkar and So [16] was adopted and modifications suggested by Sommer and So [15] to account for buoyancy forces were incorporated. The transport equations for k and ϵ are, respectively,

$$\rho\left[\frac{\partial k}{\partial t}+\overline{U}_j\frac{\partial k}{\partial x_j}\right]=\frac{\partial}{\partial x_j}\left[\left(\mu+\frac{\mu_t}{\sigma_k}\right)\frac{\partial k}{\partial x_j}\right]+\rho P_k+\rho G_k-\rho\epsilon, \tag{5}$$

$$\rho\left[\frac{\partial \epsilon}{\partial t}+\overline{U}_j\frac{\partial \epsilon}{\partial x_j}\right]=\frac{\partial}{\partial x_j}\left[\left(\mu+\frac{\mu_t}{\sigma_\epsilon}\right)\frac{\partial \epsilon}{\partial x_j}\right]+C_{\epsilon1}\rho\frac{\epsilon}{k}P_k-C_{\epsilon2}\rho\frac{\epsilon\tilde{\epsilon}}{k}+C_{\epsilon3}\rho\frac{\epsilon}{k}G_k+\rho\xi. \tag{6}$$

In these equations, the production term due to the interaction between the mean and the turbulence fields P_k, the buoyancy-induced generation term G_k, and the near-wall correction function ξ which provides the correct behavior of ϵ in the region close to the wall are

$$P_k=-\overline{u_iu_j}\frac{\partial \overline{U}_i}{\partial x_j}, \tag{7}$$

$$G_k=-g_i\beta\overline{u_it}, \tag{8}$$

$$\xi=f_{w1}\left[-0.57\frac{\epsilon\tilde{\epsilon}}{k}+0.5\frac{\overline{\epsilon}^2}{k}-1.5C_{\epsilon1}\frac{\epsilon}{k}P_k-C_{\epsilon3}\frac{\epsilon}{k}G_k-2\frac{\nu}{\alpha+\nu}g_i\beta\epsilon_{it}\right], \tag{9}$$

where $\epsilon_{it}=0.5[1+(1/Pr)](\epsilon/k)(\overline{u_it}+n_kn_i\overline{u_kt})$.

The turbulent momentum diffusivity is formulated in terms of k and ϵ as

$$\nu_t=C_\mu f_\mu\frac{k^2}{\epsilon}, \tag{10}$$

where f_μ is a damping function which incorporates viscous effects into the turbulent stresses. Away from the wall f_μ has a value of 1 and it tends to zero in the region near the wall. It is given by

$$f_\mu=\left[1+\frac{3}{Re_t^{3/4}}\right][1+80\exp(-Re_t)]\times\left[1-\exp\left(-Re_\epsilon/43-Re_\epsilon^2/330\right)\right]. \tag{11}$$

The model coefficients for the k–ϵ model are as follows:

σ_k	σ_ϵ	C_μ	$C_{\epsilon1}$	$C_{\epsilon2}$	$C_{\epsilon3}$
1.0	1.45	0.09	1.5	1.83	1.5

Some comments regarding the velocity field modeling are warranted. First, the external and structural effects suggested by Petukhov and Polyakov [6] are embodied in $(\rho-\rho_0)$ in Eq. (2) and G_k in Eq. (5), respectively. Second, calculating the turbulent stresses using Eq. (4) may not be adequate since anisotropy cannot be accounted for and no distinction can be made between the R_m and R_0 locations. Use of explicit algebraic Reynolds stress models [17] was pursued to remedy this inadequacy. The results obtained were discouraging however.

2.2.2. Thermal field

To close the thermal energy equation it is necessary to provide the turbulent heat flux components. These

can be related to the corresponding gradients of the mean fluid temperature by invoking the eddy diffusivity concept

$$\overline{u_i t} = -\alpha_t \frac{\partial \overline{T}}{\partial x_i}. \tag{12}$$

Thus, an expression for turbulent thermal diffusivity α_t has to be supplied to obtain $\overline{u_i t}$. We calculated it in terms of the time scales of the turbulent velocity field k/ϵ and the thermal field $\overline{t^2}/\epsilon_t$, along with the velocity scale $k^{1/2}$

$$\alpha_t = C_\lambda f_\lambda k \sqrt{\frac{k}{\epsilon}\frac{\overline{t^2}}{\epsilon_t}}, \tag{13}$$

where the damping function f_λ, which represents the attenuation effect in the near-wall region, is

$$f_\lambda = \frac{C_{\lambda 1}(1 - f_{\lambda 1})}{Re_t^{1/4}} + f_{\lambda 1} \tag{14}$$

and $f_{\lambda 1} = [1 - \exp(y^+/A^+)]^2$.

The thickness of the molecular thermal layer in comparison to that of the viscous layer depends on the Prandtl number of the fluid, determining where the turbulent transport of heat exceeds its molecular diffusion. As such, the Prandtl number needs to be incorporated into the damping function f_λ. In the model, this characteristic is represented by A^+ and $C_{\lambda 1}$ which contain the Prandtl number as a parameter: $A^+ = 10/Pr$ for $Pr < 0.25$ and $A^+ = 39/Pr^{1/16}$ for $Pr \geqslant 0.25$; $C_{\lambda 1} = 0.4/Pr^{1/4}$ for $Pr < 0.1$ and $C_{\lambda 1} = 0.07/Pr$ for $Pr \geqslant 0.1$.

The temperature variance and its dissipation rate were calculated by the two-equation model of So and Sommer [12]. The transport equations are

$$\rho\left[\frac{\partial \overline{t^2}}{\partial t} + \overline{U}_j \frac{\partial \overline{t^2}}{\partial x_j}\right] = \frac{\partial}{\partial x_j}\left[\rho\left(\alpha + \frac{\alpha_t}{\sigma_t}\right)\frac{\partial \overline{t^2}}{\partial x_j}\right] + 2\rho P_t - 2\rho\epsilon_t, \tag{15}$$

$$\begin{aligned}\rho\left[\frac{\partial \epsilon_t}{\partial t} + \overline{U}_j \frac{\partial \epsilon_t}{\partial x_j}\right] &= \frac{\partial}{\partial x_j}\left[\rho\left(\alpha + \frac{\alpha_t}{\sigma_{\epsilon t}}\right)\frac{\partial \epsilon_t}{\partial x_j}\right] \\ &\quad + C_{d1}\rho\frac{\epsilon_t}{\overline{t^2}}P_t + C_{d2}\rho\frac{\epsilon}{k}P_t \\ &\quad + C_{d3}\rho\frac{\epsilon_t}{k}P_k - C_{d4}\rho\frac{\widetilde{\epsilon_t}}{\overline{t^2}}\epsilon_t \\ &\quad - C_{d5}\rho\frac{\tilde{\epsilon}}{k}\epsilon_t + \rho\xi_{\epsilon t},\end{aligned} \tag{16}$$

where the production term P_t and the near-wall correction term $\xi_{\epsilon t}$ are given by

$$P_t = -\overline{u_k t}\frac{\partial \overline{T}}{\partial x_k}, \tag{17}$$

$$\begin{aligned}\xi_{\epsilon t} = f_{w,\epsilon t}\Bigg[&(C_{d4} - 4)\frac{\epsilon_t}{\overline{t^2}}\widetilde{\epsilon}_t + C_{d5}\frac{\tilde{\epsilon}}{k}\epsilon_t - \frac{\epsilon_t^{*2}}{\overline{t^2}} \\ &+ (2 - C_{d1} - C_{d2}Pr)\frac{\epsilon_t}{\overline{t^2}}P_t^*\Bigg].\end{aligned} \tag{18}$$

Finally, the model coefficients are as follows:

σ_t	$\sigma_{\epsilon t}$	C_λ	C_{d1}	C_{d2}	C_{d3}	C_{d4}	C_{d5}
0.75	1.0	0.096	1.8	0.0	0.72	2.2	0.8

The turbulent heat flux components are often evaluated by a gradient approximation, Eq. (12). From this and the sign of the turbulent thermal diffusivity (always positive) it is apparent that for a heated turbulent flow in which the axial temperature gradient is positive, the axial turbulent heat flux will always be predicted to be negative. As mentioned earlier, we adopted the EAHF model of So and Sommer [14] for closure of the turbulent heat flux components. This model assumes local equilibrium turbulence for the velocity and thermal fields and importantly, is asymptotically correct in the near-wall region. To account for the buoyancy effects, the modifications suggested by Sommer and So [15] were introduced in the EAHF model. The relations are

$$\begin{aligned}\overline{u_i t} = -\alpha_t\frac{\partial \overline{T}}{\partial x_i} + \frac{1}{C_{1t}}\sqrt{\frac{k}{\epsilon}\frac{\overline{t^2}}{\epsilon_t}}\Bigg\langle\{&[2\nu_t + (1 - C_{2t})\alpha_t]S_{ij} \\ &+ (1 - C_{2t})\alpha_t W_{ij}\}\frac{\partial \overline{T}}{\partial x_j} - (1 - C_{2t})g_i\beta\overline{t^2}\Bigg\rangle,\end{aligned} \tag{19}$$

where the model coefficients are $C_{1t} = 3.28$ and $C_{2t} = 0.4$.

The wall boundary conditions were as follows. For the momentum equation, the no-slip condition at the inner and outer walls were used. For k and ϵ, they were, respectively, $k_w = 0$ and $\epsilon_w = \nu\left(\partial k^{1/2}/\partial y\right)^2$.

A constant heat flux at the inner wall and an adiabatic outer wall were the boundary conditions for the thermal energy equation in the heated length of the channel. The wall boundary conditions for $\overline{t^2}$ and ϵ_t were, respectively,

$$\left(\overline{t^2}\right)_w = 0 \quad \text{and} \quad (\epsilon_t)_w = \alpha\left[\partial\left(\overline{t^2}\right)^{1/2}\Big/\partial y\right]^2.$$

All thermodynamic properties of the fluid were evaluated using the static pressure and temperature fields.

3. Method of solution

The flow was assumed to be axisymmetric. The governing equations were discretized using a finite difference scheme whose accuracy is second-order in space and time in a structured staggered grid. The discretized equations were solved by means of the fractional step method [18,19]. The momentum, thermal energy and turbulence model equations were solved by a time-marching algorithm. The convective part of the equations was solved by the method of characteristics and the

diffusion part was treated implicitly. For mass conservation, a Poisson equation for the pressure was solved.

In reference to Fig. 1, a total length of 2.99 m was simulated of which the first 0.91 m was unheated while the remaining 2.08 m was heated. It was not feasible to simulate the entire length at one time due to computer memory restrictions. As such, the channel was divided into 13 subsections, each 25 cm long.[1] Each subsection represented the computational domain for one simulation. This approach has a drawback – if there existed disturbances downstream of a given subsection, they could not affect the subsection. In other words, the simulation procedure rendered the Navier–Stokes equations quasi-parabolic. In each subsection, 49 radial grid points were used and they were allocated in such a manner that the point closest to the wall was at $y^+ < 1$ for both walls. The distance between two successive grid points was incremented away from the wall at a ratio of about 1.23. The axial mesh size was uniform and equal to 0.0005 m. Three grid points were used in the azimuthal direction such that $\phi_{j+1} - \phi_j = \pi/320$.

A small overlap length between the end of a subsection and the beginning of the one immediately downstream was provided in order that the inlet condition specified for the downstream subsection was the computed result slightly upstream of the upstream subsection outlet. This was done in order that perturbations, if any, in the results at a subsection outlet did not disturb the computation downstream.

The channel unheated length was represented by four subsections. Flat profiles for the mean velocity, the turbulent kinetic energy, and its dissipation rate were the inlet conditions specified for the first unheated subsection. The turbulent kinetic energy was assumed to be a fraction of the mean flow kinetic energy such that $u'_c/\overline{U}_b$ was about 10% and the dissipation rate was taken to be $\epsilon_{in} = k_{in}^{3/2}/\ell$, ℓ being equal to $0.05D_h$. To ensure that the results were independent of the inlet conditions for k and ϵ, $u'_c/\overline{U}_b$ was varied between 5% and 15% and ℓ between $0.02D_h$ and $0.1D_h$. For these ranges of values, no discernible changes in the results could be observed.

For the first heated subsection, the inlet conditions for the temperature variance and its dissipation rate were prescribed as

$$\overline{t^2} = \overline{t^2}^{++} T_\tau^{++2} \text{ and } \epsilon_t = \epsilon_t^{++} T_\tau^{++2} U_\tau^2/\nu,$$

where

$$\overline{t^2}^{++} = k^+ = k/U_\tau^2,\ \epsilon_t^{++} = 0.5\epsilon^+ = 0.5\epsilon\nu/U_\tau^4 \text{ and } T_\tau^{++} = q''_w/A\rho C_P U_\tau.$$

[1] The subsection lengths add to 3.25 m. The reason is given in the next paragraph.

A is a constant and its value must be between 50 and 100 [20]. The value of this constant was set at 75 in our simulations.

The outlet boundary conditions in all cases were $\partial\psi/\partial z = 0$, where ψ is any field variable. The convergence criterion was

$$\frac{\sum \left(\psi^{n+1} - \psi^n\right)^2}{\sum \left(\psi^{n+1}\right)^2} < 10^{-6}. \tag{20}$$

All the simulations reported were performed in a CRAY C98 computer at Electricité de France.

4. Results and discussion

The conditions and experiment numbers for the simulations reported here are given in Table 1 of Part I of this two-part paper [21]. In the figures that follow, the numerical results are represented by lines and the experimental measurements by symbols.

4.1. Isothermal flow

Figs. 2(a)–(c) show, respectively, the radial profiles at the measurement plane of mean axial velocity, turbulent kinetic energy, and axial Reynolds shear stress, and their comparison with our measurements [21]. The calculated results and the experimental data have been normalized by the mean axial bulk velocity at the channel inlet.

It is well known that when Reynolds number increases the mean axial velocity profile becomes flatter and its radial gradient increases in the near-wall region. This behavior can be observed in both the experimental data and the simulations. The agreement between the measurements and the simulations is good, except in the region where the mean axial velocity is maximum or near maximum, and close to the inner wall. The convex inner surface renders the measured profile fuller close to it. This feature is not predicted correctly by our model. Also, the maximum mean axial velocity according to the simulation is at $R^* \approx 0.41$ while the measured location is between 0.44 and 0.45.

The normalized turbulent kinetic energy results are shown in Fig. 2(b). Since the azimuthal velocity fluctuation intensity was not measured, it was estimated as $\overline{w^2} = 1.5\overline{v^2}$ on the basis of the measurements of Brighton and Jones [22] in obtaining the experimental turbulent kinetic energy. Both the measurement and simulation results indicate that the ratio $k/\overline{U}_b^2$ decreases as Re increases. In the simulations, the location of the peak in the turbulent kinetic energy shifts towards the wall with increasing Re. This feature can not be seen in the measurements because the wall was not approached closely enough ($R^* \gtrsim 0.019, y^+ \gtrsim 15$–$25$). The location of minimum k is at about the same as where the mean axial

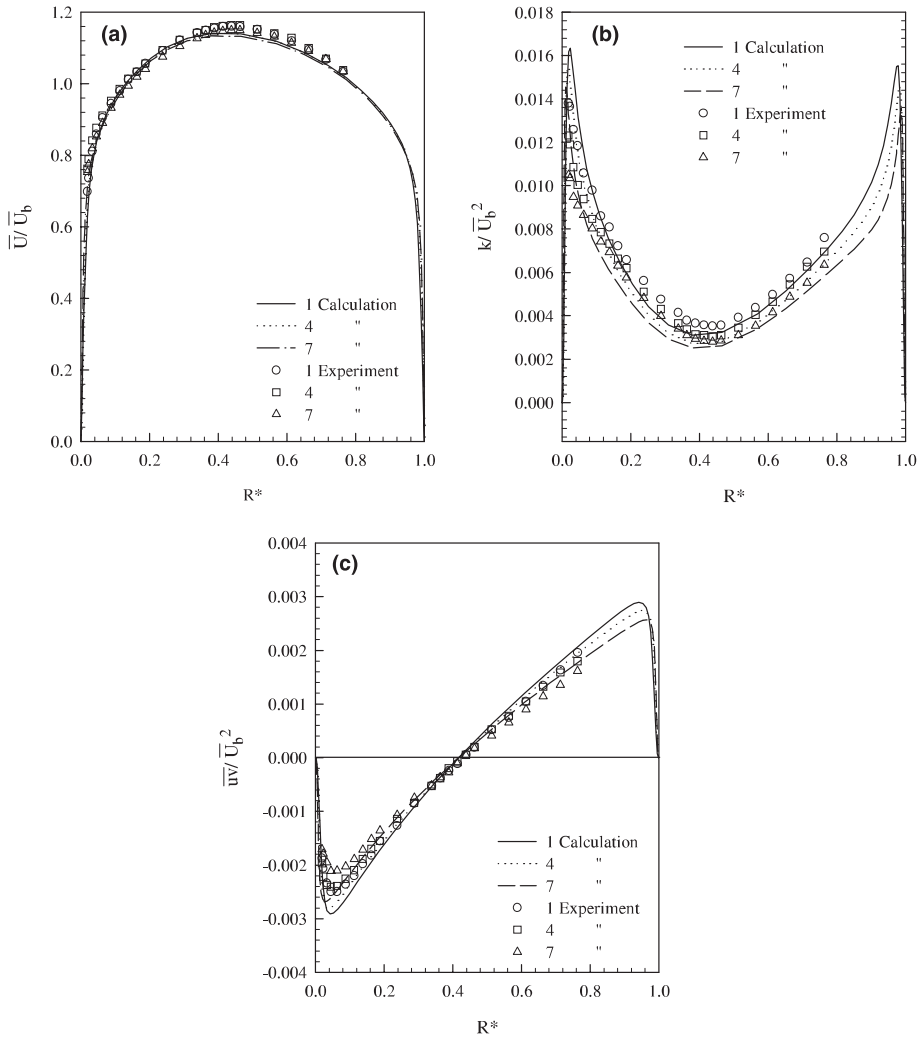

Fig. 2. Results for isothermal flow: (a) mean axial velocity; (b) turbulent kinetic energy; (c) axial turbulent shear stress (divided by ρ).

velocity is maximum. Except in the region close to the inner wall, the agreement between the calculated and experimental data is good. It should be mentioned that the estimate for $\overline{w^2}$ used in obtaining the measured k may not be appropriate in the near-wall region since the anisotropy in the turbulent normal stresses increases here [22].

Fig. 2(c) shows the axial turbulent shear stress distributions. The calculated turbulent shear stress distributions are consistently larger in magnitude than the measured ones. The location near the inner wall where the axial Reynolds shear stress reaches its maximum magnitude shifts towards the wall as *Re* increases in both the measurements and the simulations, this displacement being more evident in the calculations. Since $\overline{uv}$ is obtained in the simulations via the gradient transport approximation, Eq. (4), the location where the calculated shear stress is zero is the same as that where the mean axial velocity is maximum, i.e., $R_0^* \simeq 0.41$. In contrast, the measured value of R_0^* is between 0.42 and 0.43, i.e., the calculated location is slightly closer to the inner wall than the *measured* location. It is noteworthy that neither the experimental nor the calculated zero shear stress location changes in the Reynolds number range considered. An axial momentum balance in the channel yields the relation

$$\frac{\tau_{wi}}{\tau_{wo}} = \frac{r_o\left(R_0^2 - r_i^2\right)}{r_i\left(r_o^2 - R_0^2\right)}. \tag{21}$$

Eq. (21) indicates that the ratio τ_{wi}/τ_{wo} is invariant. The ratio is found to be equal to 1.11 using the calculated value of R_0. The ratio becomes equal to 1.17 when the measured R_0 is used.

The measured maximum value of the structural parameter $(-\overline{uv}/k)^2$ – and hence C_μ – in the annular channel is 0.07. The value of this constant is 0.09 in the k–ϵ turbulence model. This may explain some of the differences between our calculations and our measurements.

4.2. Heated flow

Figs. 3–9 show the comparison between the simulation results and the measurements for heated turbulent flow in the annular channel. The velocity field quantities are presented in Figs. 3–5 while Figs. 6–9 show the quantities for the thermal field. The same three inlet Reynolds numbers are considered. Two different heat fluxes were imposed at the inner wall for the Reynolds numbers of 22 800 and 31 500. Only one wall heat flux was imposed for the Reynolds number of 46 400. For comparison, the isothermal flow results have been included in the velocity field plots.

4.2.1. Velocity field

The mean axial velocity distribution is shown in Figs. 3(a)–(c). The nonisothermal distributions are distorted with respect to the isothermal ones, the flow with the lowest Reynolds number and highest wall heat flux being distorted most pronouncedly, Fig. 3(a). At each Reynolds number, the profiles are monotonically shifted towards the heated wall with increasing wall heat flux, as is the location of the maximum mean axial velocity. Two radial regions can be identified in the calculated and measured mean axial velocity profiles. The first is the region between the inner (heated) wall and the location where the nonisothermal profile crosses the isothermal

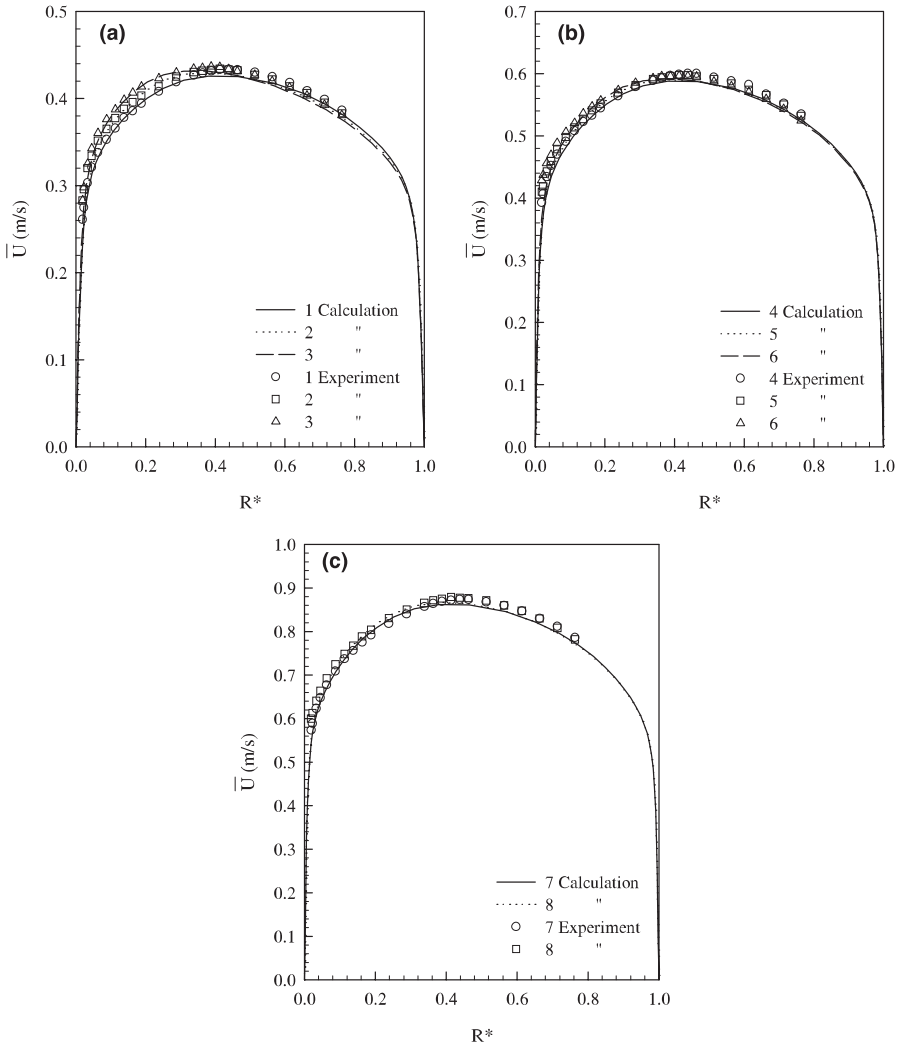

Fig. 3. Mean axial velocity for isothermal and heated flows: (a) $Re = 22\,800$; (b) $Re = 31\,500$; (c) $Re = 46\,400$.

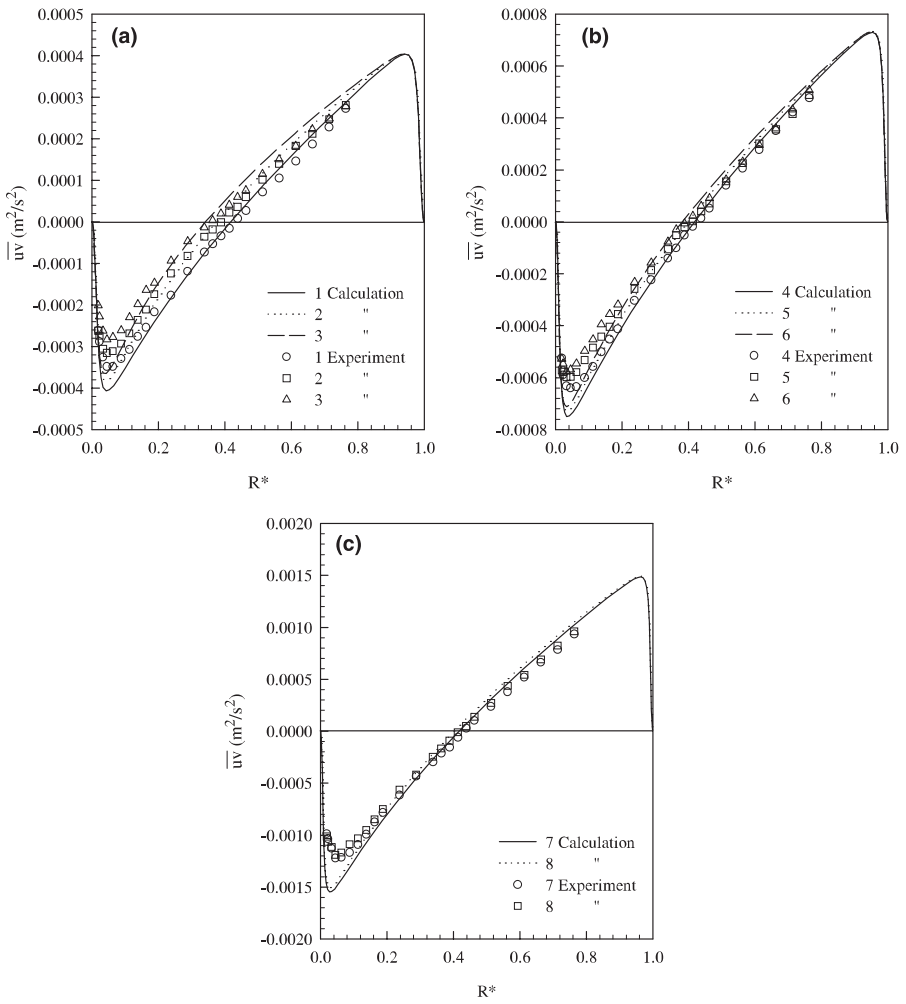

Fig. 4. Axial turbulent shear stress (divided by ρ) for isothermal and heated flows: (a) $Re = 22\,800$; (b) $Re = 31\,500$; (c) $Re = 46\,400$.

one, R_c^*. The extent of this region increases with Reynolds number at any given wall heat flux. Also, the mean axial velocity increases with the parameter Gr/Re^2 in this region. To satisfy continuity, the mean axial velocity must decrease somewhere else in the profile. This occurs in the second region which is delimited by R_c^* and the outer wall. Note that the profiles merge as the walls are approached in both regions, the locations where the merging begins being farther from the walls as the Reynolds number increases. The agreement between the simulation results and the measurements is good considering the uncertainties of the measurements.

The calculated and measured axial turbulent shear stress radial profiles are compared in Figs. 4(a)–(c), $\overline{uv}$ having been calculated as $-\nu_t(\partial\overline{U}/\partial r)$. Buoyancy modifies the balance between the forces acting on the fluid across the channel resulting in a more asymmetric distribution of $\overline{uv}$ compared to isothermal flow at the same Reynolds number. As Gr/Re^2 increases, the zero $\overline{uv}$ location shifts toward the inner wall, causing the magnitude of $\overline{uv}$ to decrease in the region $r < R_0$ and increase in the region $r > R_0$. The calculated and measured $\overline{uv}$ profiles exhibit similar trends although the calculated values are consistently larger in magnitude. The measurements indicate that the distance $(R_m - R_0)$ increases with Gr/Re^2 but this feature could not be captured in the calculations.

The turbulent kinetic energy radial profiles are shown in Figs. 5(a)–(c). As in the Part I paper, the experimental k is evaluated as $(\overline{u^2} + 2.5\overline{v^2})/2$. Both the calculated and the measured radial distributions become more asymmetric in the heated flows. The minimum-k location shifts monotonically toward the inner wall with increasing wall heat flux. In comparison to isothermal flow at a specific Reynolds number, the calculated k in the heated flow decreases in the region $0.05 < R^* < R_0^*$ and

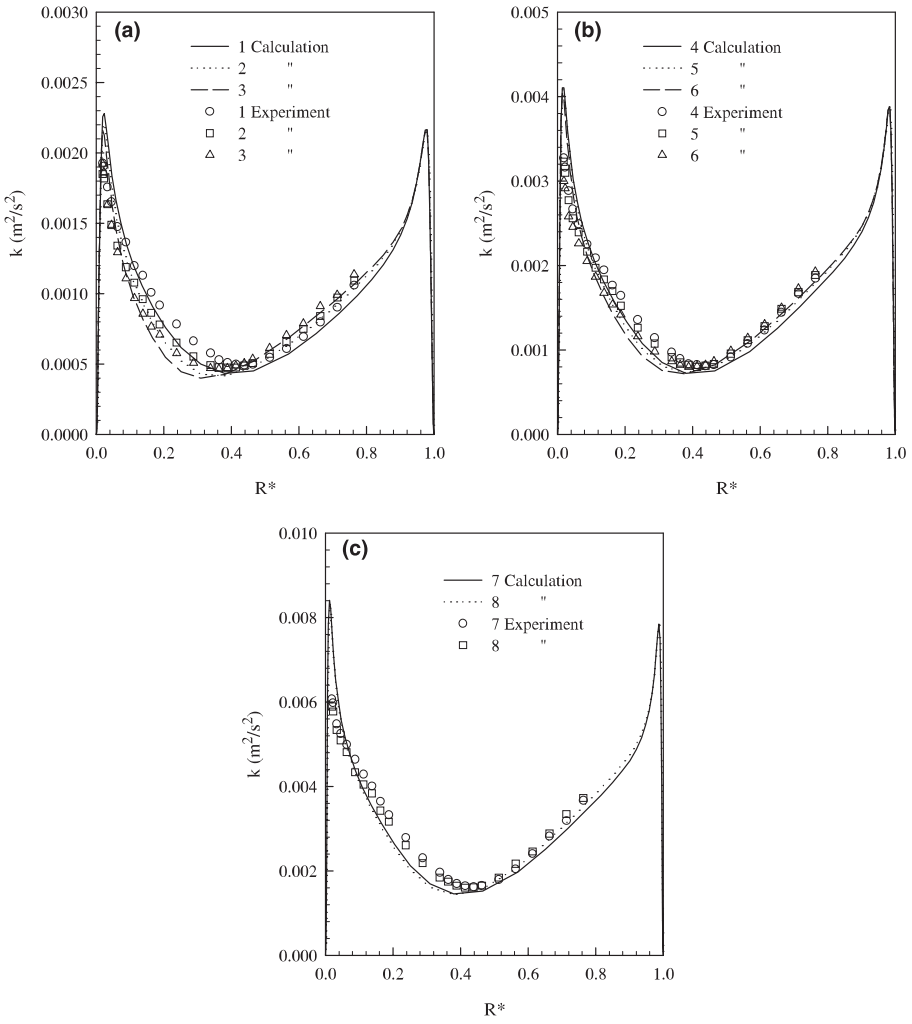

Fig. 5. Turbulent kinetic energy per unit mass of fluid for isothermal and heated flows: (a) $Re = 22\,800$; (b) $Re = 31\,500$; (c) $Re = 46\,400$.

increases in $R_0^* < R^* < 0.9$. Good agreement is seen between the calculated and measured profiles radially outboard of where k is minimum. To the left of the minimum-k location, while the measurements exhibit the same trend as the simulation results the magnitudes differ somewhat. It also appears that, at least at the present conditions, heating does not affect the distribution of k very close to the inner and outer walls in either the experiments or the simulations.

A discussion of the effect of buoyancy on the velocity field is provided in Part I of this paper. It remains pertinent to the simulation results reported here.

Recall that $\overline{uv}$ is calculated as $-\nu_t(\partial\overline{U}/\partial r)$. Some improvements will be necessary here. It may be appropriate, for instance, to introduce an additional damping function in the equation for the turbulent momentum diffusivity, Eq. (10), or add terms in Eq. (4), to properly account for the *external* and *structural* effects on the axial turbulent shear stress.

4.2.2. Thermal field

The results for the turbulent thermal field are presented in a manner different from that for the velocity field. The separate effects of *Re* and *Gr* on the calculated and the measured radial distributions of the mean temperature, temperature fluctuation intensity, and radial and axial turbulent heat fluxes are scrutinized. Some results are presented in dimensional as well as nondimensional form.

Fig. 6(a) shows the mean temperature distribution in dimensional form for the lowest inlet Reynolds number (22 800) at the two inner wall heat fluxes. The agreement between the calculated and the measured fluid temperature is good. Three values of the inner wall

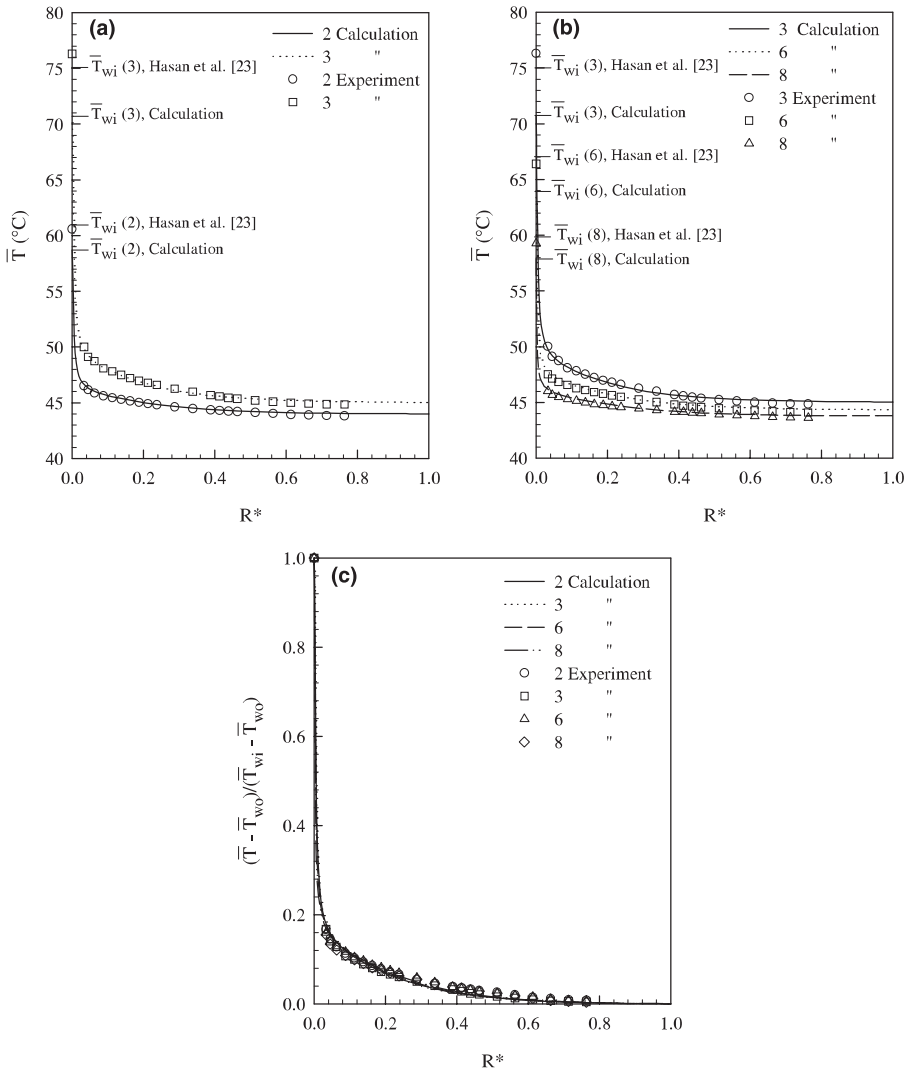

Fig. 6. Results for mean temperature: (a) $Re = 22\,800$; (b) $q''_w = 16\,000$ W/m^2; (c) nondimensional mean temperature profile.

temperature are shown for each case – the simulation value, the measured value, and the value obtained from a correlation due to Hasan et al. [23]. The simulation value for the higher wall heat flux case appears to be significantly low. The mean temperature profiles for the three inlet Reynolds numbers at inner wall heat flux of 16 000 W/m^2 are compared in Fig. 6(b). The calculated profiles exhibit some difference from the measured profiles beyond $R^* \simeq 0.4$. Fig. 6(c) shows the nondimensional mean temperature profiles for the cases shown in Figs. 6(a) and (b). In the calculated and measured distributions the molecular thermal sublayer thickness decreases when the Reynolds number increases and the nondimensional profiles becomes slightly flatter.

The effect of increasing inner wall heat flux on the temperature fluctuation intensity at inlet Reynolds number of 22 800 can be observed in Fig. 7(a). In Fig. 7(b), the calculated and measured temperature fluctuation intensity profiles at inner wall heat flux of 16 000 W/m^2 are compared for the three Reynolds numbers. The measured values are higher than the calculated values in all cases although their trends are similar. One feature of the measurement that is not captured correctly by the simulation is the close to linear distribution shown by the measured profiles over the region $0.15 \lesssim R^* \lesssim 0.4$.

The profile of radial turbulent heat flux at inlet Reynolds number of 22 800 is shown in Fig. 8(a) for the two inner wall heat fluxes. The agreement between the numerical results and the measurements is good except close to the heated wall. The undermeasurement of $\overline{vt}$ near the wall was discussed in Part I of this paper. In

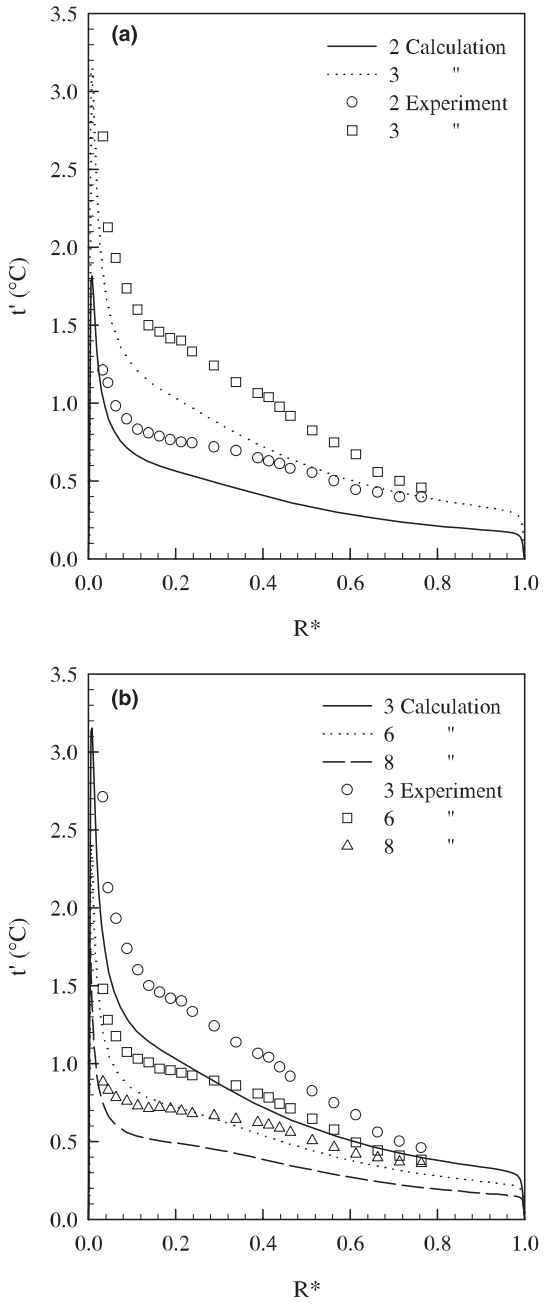

Fig. 7. Results for temperature fluctuation intensity: (a) $Re = 22\,800$; (b) $q''_w = 16\,000$ W/m^2.

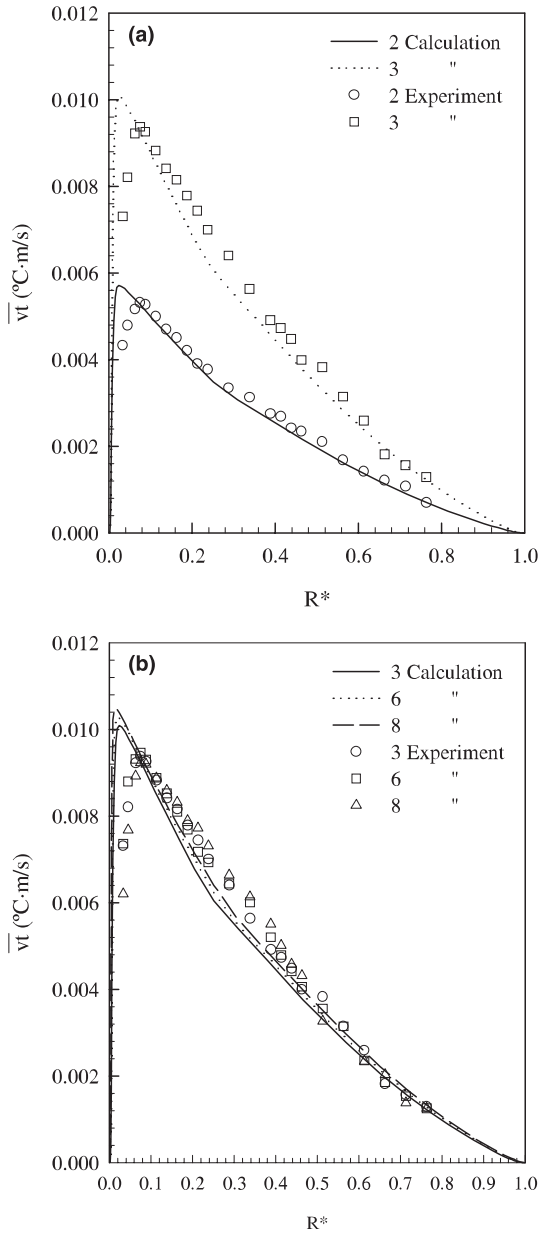

Fig. 8. Results for radial turbulent heat flux (divided by ρC_P): (a) $Re = 22\,800$; (b) $q''_w = 16\,000$ W/m^2.

Fig. 8(b), the influence of Reynolds number increase on $\overline{vt}$ at the same wall heat flux can be seen. The calculated distribution increases slightly in magnitude in the entire flow field as the Reynolds number increases with the location of its maximum shifting slightly toward the heated wall. Similar trends were reported by Petukhov and Polyakov [6] for turbulent upflow of air in a heated vertical pipe. It is not possible to decipher these small effects in the measured profiles mainly because of the uncertainty involved.

Finally, the radial distribution of the axial turbulent heat flux is presented in Figs. 9(a) and (b). The effect of increasing the wall heat flux at constant Re can be observed in Fig. 9(a). Two features are apparent in the calculated results: first, $\overline{ut}$ increases in magnitude; and second, the location, where $\overline{ut} = 0$ shifts toward the heated wall and does not necessarily coincide with the location where the mean axial velocity is maximum

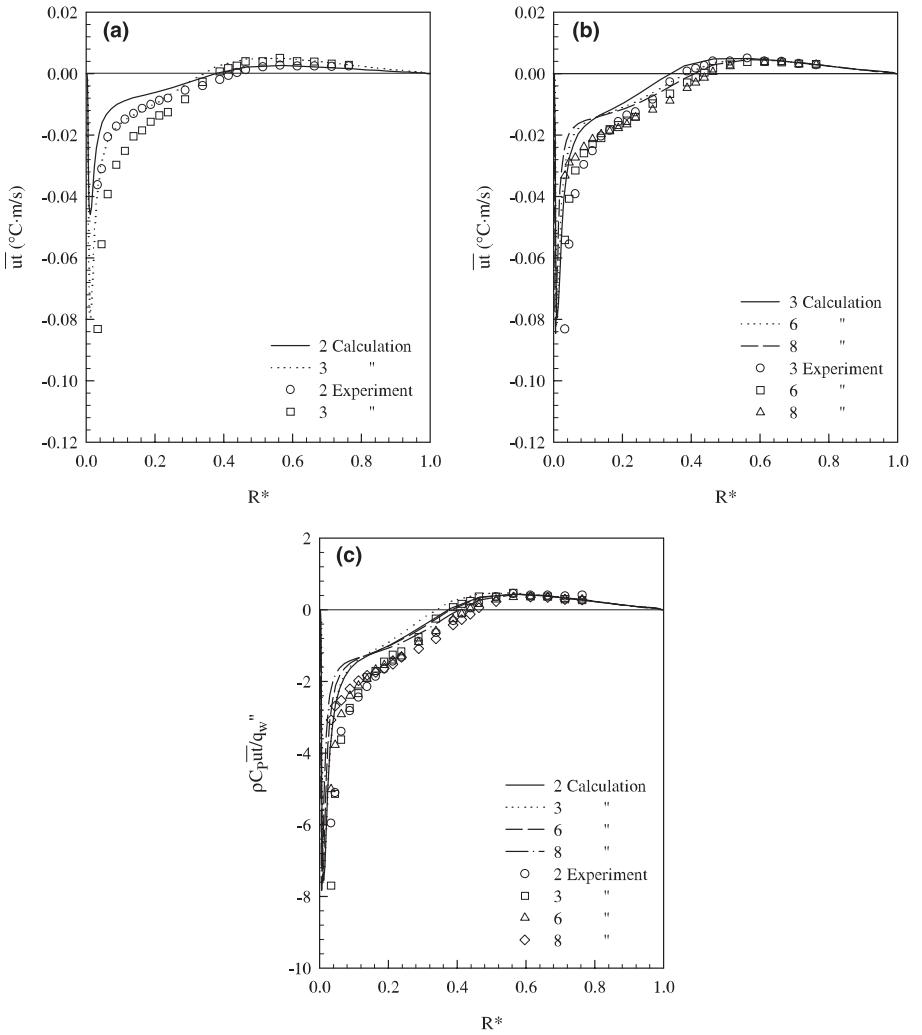

Fig. 9. Results for axial turbulent heat flux (divided by ρC_P): (a) $Re = 22\,800$; (b) $q''_w = 16\,000$ W/m^2; (c) nondimensional axial turbulent heat flux profile.

(although they are near each other) or where $\overline{uv} = 0$. Fig. 9(b) shows that if the Reynolds number increases at the same wall heat flux, the $\overline{ut} = 0$ location moves away from the heated wall. The nondimensional axial turbulent heat flux profiles are presented in Fig. 9(c). Both the calculations and the measurements show the effect of buoyancy as Gr/Re^2 increases – the nondimensional axial turbulent heat flux decreases in the vicinity of the heated wall. The reasons for this can be explained from the algebraic equation for $\overline{ut}$, Eq. (19). Buoyancy affects $\overline{ut}$ directly in the region, causing it to decrease.

5. Concluding remarks

Isothermal and heated turbulent liquid flow through a vertical concentric annular channel was simulated. At nonisothermal conditions the channel inner wall was heated and the outer wall insulated. Two near-wall two-equation turbulence models were employed for closure. A k–ϵ model was used for the velocity field and a $\overline{t^2}$–ϵ_t model for the thermal field, along with an explicit algebraic model for the turbulent heat flux components. Turbulent thermal field models that do not use the Reynolds analogy may allow a more realistic simulation of the flow field and this is demonstrated in the results obtained. The use of the algebraic heat flux model also made it possible to correctly calculate the production terms due to buoyancy in the k–ϵ turbulence model.

Generally, the numerical model successfully predicted the key features of the flow including the buoyancy effects that had been observed experimentally upon imposition of wall heating.

Acknowledgements

This research was supported by National Science Foundation, Thermal Systems Program, Division of Chemical and Thermal Systems, under Grant No. CTS-9411898. Funding from Electric Power Research Institute and Electricité de France is also gratefully acknowledged. Funding for J.A. Zarate was provided by Consejo Nacional de Ciencia y Tecnologia, Mexico.

References

[1] A. Quarmby, An analysis of turbulent flow in concentric annuli, Appl. Sci. Res. 19 (1968) 250–271.
[2] K. Hanjalic, Prediction of turbulent flow in annular ducts with differential transport model of turbulence, Wärme Stoffübertragung 7 (1974) 72–78.
[3] I. Azous, S.A. Shirazi, A. Pilehvari, J.J. Azar, Numerical simulation of turbulent flow in concentric and eccentric annuli, AIAA Paper 93-3106, 1993.
[4] N.W. Wilson, J.O. Medwell, An analysis of heat transfer for fully developed turbulent flow in concentric annuli, ASME J. Heat Transfer 90C (1968) 43–50.
[5] M.J. Malik, R.H. Pletcher, A study of some turbulence models for flow and heat transfer in ducts of annular cross-section, ASME J. Heat Transfer 103 (1981) 146–152.
[6] B.S. Petukhov, A.F. Polyakov, in: B.E. Launder (Ed.), Heat Transfer in Turbulent Mixed Convection, Hemisphere, Washington, DC, 1988.
[7] A.M. Abdelmeguid, D.B. Spalding, Turbulent flow and heat transfer in pipes with buoyancy effects, J. Fluid Mech. 94 (1979) 383–400.
[8] J.R. Pietrzyk, M.E. Crawford, A numerical investigation of turbulent mixed convection in vertical annular channels, in: Fundamentals of Forced and Mixed Convection ASME HTD 42, New York, 1985, pp. 149–158.
[9] M.A. Cotton, J.D. Jackson, Vertical tube air flows in the turbulent mixed convection regime calculated using a k–ϵ model, Int. J. Heat Mass Transfer 33 (1990) 275–286.
[10] W.M. Kays, Turbulent Prandtl number – where are we? ASME J. Heat Transfer 116 (1994) 284–295.
[11] N. Kasagi, Direct numerical simulation data bases: an effective tool in fundamental studies of turbulent heat transfer, in: W. Nakayama, K. Yang (Eds.), Computers and Computing in Heat Transfer, Science and Engineering, CRC Press, Boca Raton, 1993, pp. 97–117.
[12] R.M.C. So, T.P. Sommer, A near-wall eddy conductivity model for fluids with different Prandtl numbers, ASME J. Heat Transfer 116 (1994) 844–854.
[13] M.S. Youssef, Y. Nagano, M.A. Tagawa, A two-equation heat transfer model for predicting turbulent thermal fields under arbitrary wall thermal conditions, Int. J. Heat Mass Transfer 35 (1992) 3095–3104.
[14] R.M.C. So, T.P. Sommer, An explicit algebraic heat-flux model for the temperature field, Int. J. Heat Mass Transfer 39 (1996) 455–465.
[15] T.P. Sommer, R.M.C. So, Wall-bounded buoyant turbulent flow and its modeling, Int. J. Heat Mass Transfer 39 (1996) 3595–3606.
[16] A. Sarkar, R.M.C. So, A critical evaluation of near-wall two-equation models against direct numerical simulation data, Int. J. Heat Fluid Flow 18 (1997) 197–208.
[17] S.S. Girimaji, Fully explicit and self-consistent algebraic Reynolds stress models, Theoret. Comput. Fluid Dyn. 8 (1996) 387–402.
[18] N.N. Yanenko, The Method of Fractional Steps, 1st ed., Springer, Berlin, 1971.
[19] E. Deutsch, W. Méchitoua, J.D. Mattéi, Flow simulation in piping system dead legs using second moment closure and k–ϵ model, in: C.J. Chen, C. Shih, J. Lienan, R.J. Kung (Eds.), Flow Modeling and Turbulence Measurements VI, A.A. Balkena, The Netherlands, 1996, pp. 277–284.
[20] T.P. Sommer, Near-wall modeling of turbulent heat transport in nonbuoyant and buoyant flows, Ph.D. thesis, Arizona State University, Tempe, AZ, 1994.
[21] S. Kang, B. Patil, J.A. Zarate, R.P. Roy, Isothermal and heated turbulent upflow in a vertical annular channel – Part I. Experimental measurements, Int. J. Heat Mass Transfer 44 (2001) 1171–1184.
[22] J.A. Brighton, J. Jones, Fully developed turbulent flow in annuli, J. Basic Eng. 86 (1964) 835–844.
[23] A. Hasan, R.P. Roy, S.P. Kalra, Heat transfer measurements in turbulent liquid flow through a vertical annular channel, ASME J. Heat Transfer 112 (1990) 247–250.